Atomistic Mechanisms and Dynamics of Adhesion, Nanoindentation, and Fracture

Uzi Landman; W. D. Luedtke; Nancy A. Burnham; Richard J. Colton

Science, New Series, Vol. 248, No. 4954 (Apr. 27, 1990), 454-461.

Stable URL:
http://links.jstor.org/sici?sici=0036-8075%2819900427%293%3A248%3A4954%3C454%3AAMADOA%3E2.0.CO%3B2-7

Science is currently published by American Association for the Advancement of Science.

Atomistic Mechanisms and Dynamics of Adhesion, Nanoindentation, and Fracture

UZI LANDMAN, W. D. LUEDTKE, NANCY A. BURNHAM, RICHARD J. COLTON

Molecular dynamics simulations and atomic force microscopy are used to investigate the atomistic mechanisms of adhesion, contact formation, nanoindentation, separation, and fracture that occur when a nickel tip interacts with a gold surface. The theoretically predicted and experimentally measured hysteresis in the force versus tip-to-sample distance relationship, found upon approach and subsequent separation of the tip from the sample, is related to inelastic deformation of the sample surface characterized by adhesion of gold atoms to the nickel tip and formation of a connective neck of atoms. At small tip-sample distances, mechanical instability causes the tip and surface to jump-to-contact, which in turn leads to adhesion-induced wetting of the nickel tip by gold atoms. Subsequent indentation of the substrate results in the onset of plastic deformation of the gold surface. The atomic-scale mechanisms underlying the formation and elongation of a connective neck, which forms upon separation, consist of structural transformations involving elastic and yielding stages.

UNDERSTANDING THE ATOMISTIC MECHANISMS, ENERGETICS, and dynamics underlying the interactions and physical processes that occur when two materials are brought together (or separated) is fundamentally important to basic and applied problems such as adhesion (*1–7*), contact formation (*3–16*), surface deformations (*7, 16, 17–24*), materials elastic and plastic response characteristics (*17–24*), materials hardness (*25–27*), microindentation (*6, 10, 26–29*), friction and wear (*16, 19, 30–32*), and fracture (*33–34*). These considerations have motivated for over a century (*1, 3, 17–20*) extensive theoretical and experimental research endeavors of the above phenomena and their technological consequences. Most theoretical approaches to these problems, with a few exceptions (*7, 14–16*), have been anchored in continuum elasticity and contact mechanics (*17–25*). Similarly, until quite recently (*35–38*) experimental observations and measurements of surface forces and the consequent materials response to such interactions have been macroscopic in nature.

The everlasting quest to understand and observe natural phenomena on refined microscopic scales has led to the development of conceptual and technological devices allowing the interrogation of materials with increasing resolution. On the experimental front the developments of the surface force apparatus (SFA) (*36*), of scanning tunneling microscopy (STM) (*37*), and of the related atomic force microscopy (AFM) (*35*) broaden our perspectives and abilities to probe the morphology, electronic structure, and nature of interatomic forces in materials, as well as enhance our ability to manipulate materials on the atomic scale (*38*).

On the theoretical front, recent advances in the formulation and evaluation of the energetics and interatomic interactions in materials (*7, 39*), coupled with the development and implementation of computational methods and simulation techniques (*7, 40*), open new avenues for investigations of the microscopic origins of complex materials phenomena. In particular large-scale molecular dynamics computer simulations, which are in a sense computer experiments, where the evolution of a system of interacting particles is simulated with high spatial and temporal resolution by means of direct integration of the particles' equations of motion, have greatly enhanced our understanding of a broad range of materials phenomena.

Although our knowledge of interfacial processes occurring when two material bodies are brought together has significantly progressed since the original presentation by Heinrich Hertz before the Berlin Physical Society in January 1881 of his theory of the contact of elastic bodies (*17*), full microscopic understanding of these processes is still lacking. Moreover, it has been recognized that continuum mechanics is not fully applicable as the scale of the material bodies and the characteristic dimension of the contact between them are reduced (*24, 41*). Furthermore, it had been observed (*19, 27*) that the mechanical properties of materials exhibit a strong dependence on the size of the sample (small specimens appear to be stronger than larger ones). Since the junctions between contacting solids can be small, their mechanical properties may be drastically different from those of the same materials in their bulk form. Consequently, the application of the newly developed theoretical and experimental techniques to these problems promises to provide significant insights concerning the microscopic mechanisms and the role of surface forces in the formation of microcontacts and to enhance our understanding of fundamental issues pertaining to interfacial adherence, microindentation, structural deformations, and the transition from elastic to elastoplastic or fully developed plastic response of materials. Additionally, studies such as those described in this paper allow critical assessment of the range of validity of continuum-based theories of these phenomena and could inspire improved analytical formulations. Finally, knowledge of the interactions and atomic-scale processes occurring between small tips and materials surfaces, and their consequences, is of crucial importance to optimize, control, interpret, and design experiments employing the novel tip-based microscopies (*6, 7, 13, 14, 16, 32, 35–38, 42–47*).

U. Landman and W. D. Luedtke are in the School of Physics, Georgia Institute of Technology, Atlanta, GA 30332. N. A. Burnham and R. J. Colton are in the Surface Chemistry Branch, Code 6177, Naval Research Laboratory, Washington, DC 20375–5000.

To this end we investigate in this paper theoretically (7) and experimentally (6) the interactions between a metallic tip (Ni) and a gold surface, chosen mainly because of differences in their mechanical properties, such as elastic moduli, yield, hardness, and strength parameters [for example, the elastic moduli are 21×10^{10} N/m^2 and 8.2×10^{10} N/m^2 for Ni and Au, respectively (48)]. The theoretical studies employed molecular dynamics (MD) simulations (7, 16) with interatomic interactions described by means of the many-body potentials obtained by the embedded-atom method (49, 50) which have been recently applied with significant success in studies of bulk and surface properties of a number of metallic systems and their alloys. The experimental measurements were performed using AFM configured to measure the force between a tip mounted on a cantilever and the sample surface as a function of tip-to-sample separation (6, 47).

Our theoretical simulations reveal the onset of an instability as the tip approaches the sample causing a jump-to-contact (JC) such as described first (14) with calculations employing Lennard-Jones (LJ) potentials and further investigated more recently with different potentials for nickel (15) and other materials (7). We find that for our system the JC phenomenon is associated primarily with a tip-induced sample deformation, which begins when the distance between the proximal atomic layers of the two interfacing materials is approximately 4.2 Å (that is, at a separation larger than the equilibrium crystalline interlayer spacings), and that the process involves large atomic displacements (~2 Å) occurring over a short time span of ~1 ps. Furthermore, we discovered that lifting the tip from the surface after contact results in an inelastic deformation of the sample exhibiting ductile extension and the eventual tear, or fracture, of the topmost Au layer which adheres to the Ni tip. The above processes are portrayed in both the results of the simulations and measurements as a marked hysteresis in the force versus distance relationship recorded along the axis of the tip-sample approach/separation. In fact, the process of tear, observed in the simulations during tip-sample separation, is akin to mode-I ductile fracture (33) (that is, load normal to the fracture plane). Allowing the tip to further advance and penetrate the sample surface beyond the point of contact indents the surface and results in further deformation of the sample characterized by an adhesion-induced flow of gold atoms which wet the edges of the Ni tip, generation of slip planes in the Au lattice, and formation of point defects. Separating the tip and sample causes the sample to deform ductilely, producing an extended crystalline "neck" that stretches between the sample and adherent layers on the tip until the neck eventually breaks. Throughout much of the elongation process the neck maintains a crystalline layered structure while reducing in cross-sectional area as it extends. The elongation mechanism revealed by the simulations consists of a sequence of elastic and plastic (yielding) stages accompanied by atomic structural rearrangement. Based on the above observations we associate the calculated and measured hysteresis in the force versus distance curves with the formation, stretching, and breaking of bonds due to adhesion, cohesion, and decohesion, and with inelastic deformations induced by the tip-to-substrate interaction.

Methodology

Prior to the presentation of our results we provide pertinent details of our studies, noting common as well as distinguishing characteristics between the theoretical and experimental modes of investigation.

Molecular dynamics simulations. Molecular dynamics simulations were performed for an Au (001) sample containing three static (bottom) and eight dynamic layers, each consisting of 450 atoms per layer. The sample interacts with a dynamic Ni tip consisting of 1400 atoms arranged originally as a pyramidal (tapered) tip with the bottom layer (closest to the sample) consisting of 72 atoms exposing a (001) surface, the next layer consisting of 128 atoms and the remaining six layers containing 200 atoms each. This gives the tip an effective radius of curvature of ~30 Å (which is approximately 50 to 100 times smaller than the tip employed in the experiment). In addition the tip interacts with a static Ni holder consisting of 1176 atoms arranged in three (001) layers. The simulations were performed at 300 K with temperature control imposed only on the deepest dynamic layer of the Au sample closest to the static layers. No significant variations in temperature were observed during the simulations. The equations of motion were integrated using a 5th order predictor-corrector algorithm with a time step $\Delta t = 3.05$ fs.

The interatomic interactions that govern the energetics and dynamics of our system are modeled by means of the embedded-atom method (EAM) (49, 50) which has been applied recently with significant success to study equilibrium and nonequilibrium properties and processes in metallic elemental and alloy systems (49–52). In this method, the dominant contribution to the cohesive energy of the material is viewed as the energy to embed an atom into the local electron density provided by other atoms of the system. This background density is determined for each atom as the superposition of electronic densities from the other atoms, evaluated at the location of the atom in question. Thus, the total cohesive energy is represented in the EAM by a many-body embedding functional, supplemented by parametrized short-range pair interactions due to inter-core repulsion. The parameters of the pair-potentials are determined via fitting to a number of bulk equilibrium properties of the metals and their alloys, such as lattice constants, heats of sublimation, elastic constants, vacancy-formation energies, and heats of solution (49, 50).

Following equilibration of the system at 300 K with the tip outside the range of interaction, the tip was lowered slowly toward the surface. For the initially equilibrated system we find multilayer relaxation (53) of the Au (001) surface, whereby the first (topmost)-to-second interlayer spacing, d_{12}, contracts by 7.5% and d_{23} expands

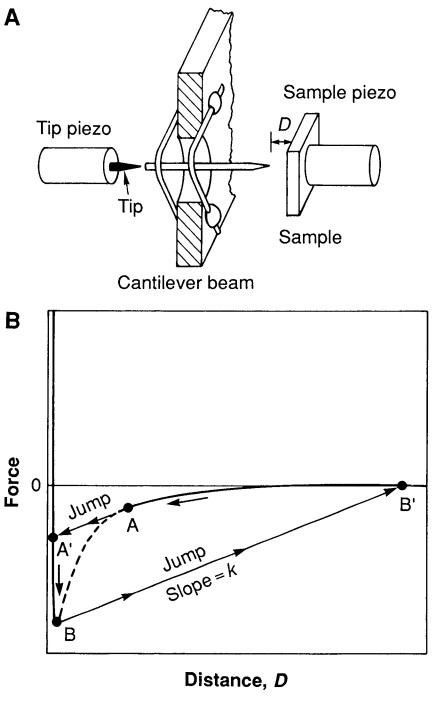

Fig. 1. (**A**) Schematic diagram showing the relative positions of the tunneling tip, cantilever tip, and sample. The tunneling tip is under feedback control, operating in the constant current mode. The piezos are used to move the tunneling tip and sample. The cantilever for this experiment was made from a piece of Ni wire bent into the shape of an "L" with a spring constant of 5000 N/m. The short part of the "L" was chemically etched into a tip with a radius of curvature of approximately 200 nm. (**B**) Schematic diagram illustrating the force measurement technique.

by 3.5% relative to the interlayer spacing in the bulk. The layer relaxation at the surface of the Ni tip is insignificant and at equilibrium the sides of the tapered part of the tip expose small (111) facets. The calculated surface energies (at 0 K) for Ni (001) and Au (001) are 1657 mJ/m^2 and 964 mJ/m^2, respectively, in close agreement with calculations (*49*) employing a slightly different parameterization of the EAM potentials.

Motion of the tip occurs by changing the position of the tip-holder assembly in increments of 0.25 Å over 500 Δt. After each increment the system is fully relaxed, that is, dynamically evolved, until no discernable variations in system properties are observed beyond natural fluctuations.

Atomic force microscope measurements. Forces may be measured experimentally with AFM (*6, 35*); both attractive and repulsive forces can be measured as well as the adhesive force necessary to separate the tip and sample surface after contact. Figure 1 depicts schematically the forces acting between the tip (which is mounted on a cantilever beam) and sample as a function of the separation D between the cantilever tip and sample. The arrows are used to guide the eye throughout the full interaction cycle. The cycle starts with the sample far away and the cantilever in its rest position. As D decreases, the cantilever bends towards the sample such that at any equilibrium separation D the attractive force, F, balances the restoring force of the cantilever defined by its effective spring constant k times its deflection. However, if the magnitude of the gradient of the attractive force dF/dD exceeds k (point A), the cantilever will jump into contact with the sample (point A′). This instability is governed by the stiffness of the cantilever beam relative to the long-range forces, while in the MD simulations, where the cantilever is modeled by a rigid tip-holder (that is, an infinitely stiff cantilever beam), the JC instability is driven by the inherent stiffness (related to the cohesive strength) of the tip and substrate materials.

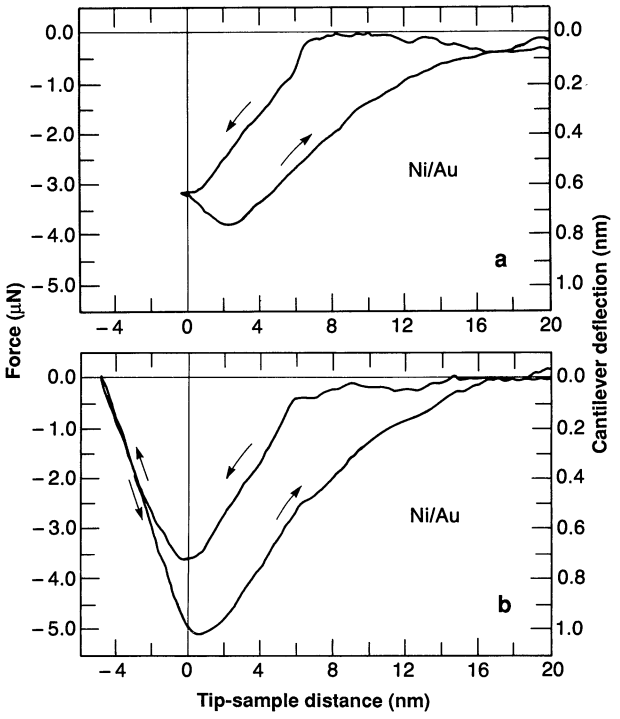

Fig. 2. Experimentally measured force versus tip-to-sample distance relationship between a Ni tip and Au sample for (**a**) contact followed by separation and (**b**) indentation followed by separation. The force curves were obtained using AFM in dry nitrogen.

On reversing the direction of the sample, the cantilever will jump away from the sample at B to some point B′ giving rise to hysteresis in the measured force curve, the magnitude of which depends on k and F. Thus in the experiment, the degree of resolution, that is, the ability to track the force versus distance curve for all tip-to-surface separations, depends on the selection of the cantilever. For example, if k is at any time less than dF/dD, the dotted segment of the interaction force curve $D_A \leq D \leq D_B$ (see Fig. 1) is inaccessible.

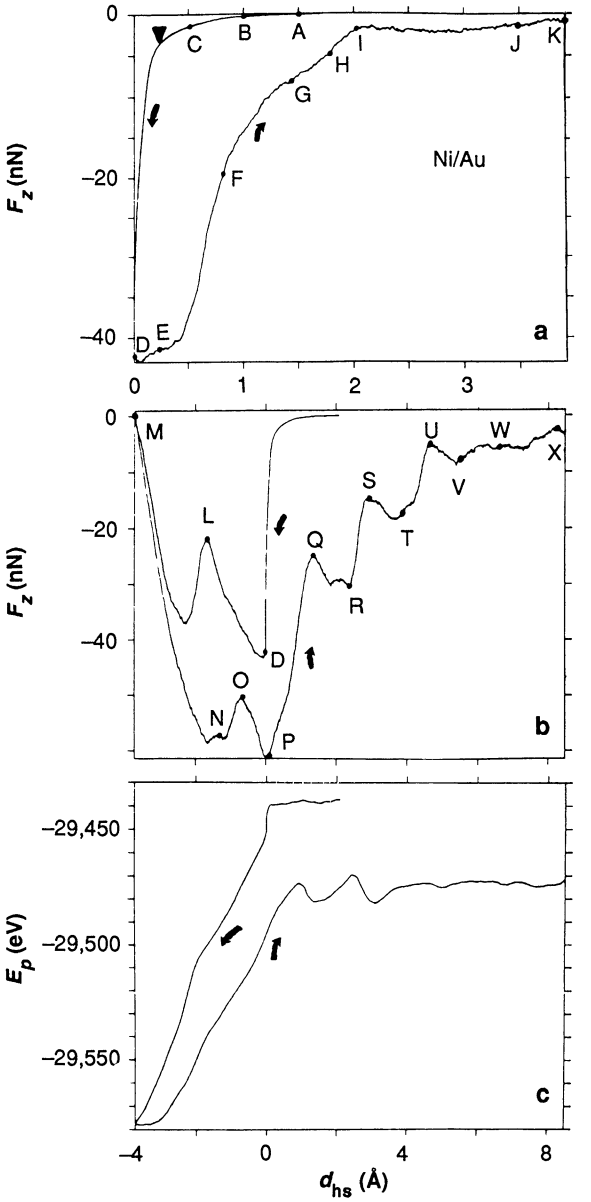

Fig. 3. Calculated force, F_z, versus tip-to-sample distance, d_{hs}, relationship between a Ni tip and an Au sample for: (**a**) approach and jump-to-contact followed by separation; (**b**) approach, jump-to-contact, indentation, and subsequent separation; d_{hs} denotes the distance between the rigid tip-holder assembly and the static substrate of the Au surface (d_{hs} = 0 at the jump-to-contact point, marked D). The capital letters on the curves denote the actual distances, d_{ts}, between the bottom part of the Ni tip and the Au surface; in (a): A = 5.7 Å, B = 5.2 Å, C = 4.7 Å, D = 3.8 Å, E = 4.4 Å, F = 4.85 Å, G = 5.5 Å, H = 5.9 Å, I = 6.2 Å, J = 7.5 Å, and K = 8.0 Å; in (b): D = 3.8 Å, L = 2.4 Å, M = 0.8 Å, N = 2.6 Å, O = 3.0 Å, P = 3.8 Å, Q = 5.4 Å, R = 6.4 Å, S = 7.0 Å, T = 7.7 Å, U = 9.1 Å, V = 9.6 Å, W = 10.5 Å, and X = 12.8 Å. (**c**) Potential energy of the system for a complete cycle of the tip approach, jump-to-contact, indentation, and subsequent separation. Forces in units of nanonewtons, energy in electron volts and distances in angstroms.

However, if k is always greater than dF/dD, as for our experiment, the cantilever-dependent instability can be practically eliminated, thus enabling a faithful measurement of the consequences of the tip-to-sample interatomic interactions and the resultant hysteresis, attributable to adhesion, in the force versus separation curve.

The AFM instrument employs a cantilever beam made from Ni wire (0.25 mm in diameter) and bent into the shape of an "L" whose long and short dimensions are approximately 6 and 2 mm, respectively. The short part of the bent wire was chemically etched with hydrochloric acid into a tip with a radius of curvature of ~200 nm as determined by scanning electron microscopy. The cantilever's spring constant is calculated to be ~5000 N/m. Its deflection is measured with a tunneling microscope. Details of the instrumentation are described elsewhere (*6*). Whereas in the simulation the tip is moved, in the experiment the sample is moved by means of a piezoelectric actuator at a rate of 5 nm/s. Sample velocity was chosen to be intermediate to the thermal drift rate (<1 nm/min) and tunneling microscope slew rate (~100 nm/s).

The AFM measurements were done in a dry box under dry nitrogen with tips and samples that were prepared in air and then quickly transferred to the dry box. The sample was an evaporated Au film (approximately 100 nm thick) that was cleaned in a solution of sodium dichromate and concentrated sulfuric acid and rinsed with distilled water until the surface was hydrophilic.

Results and Discussion

Measured and simulated force versus distance curves are shown in Figs. 2 and 3, respectively, as well as the calculated potential energy versus distance (Fig. 3c). In both cases results for tip-to-sample approach followed by separation are shown, for adhesive contact (Figs. 2a and 3a) and indentation (Figs. 2b and 3, b and c) studies. As discussed above, the simulations correspond to a case of a rigid cantilever and therefore the recorded properties of the system as the tip-holder assembly approaches or retracts from the sample portray directly consequences of the interatomic interactions between the tip and the sample. The distance scale that we have chosen in presenting the calculated results is the separation (denoted as d_{hs}) between the rigid (static) holder of the tip and the static gold lattice underlying the dynamic substrate. The origin of the distance scale is chosen such that $d_{hs} = 0$ after JC occurs ($d_{hs} \geq 0$ when the system is not advanced beyond the JC point and $d_{hs} < 0$ corresponds to indentation). Since the dynamic Ni tip and Au substrate atoms displace in response to the interaction between them, the distance d_{hs} does not give directly the actual separation between regions in the dynamic tip and substrate material. The actual relative distances, d_{ts}, between the bottom part of the tip (averaged z-position of atoms in the bottommost layer of the tip) and the surface (averaged z-position of the topmost layer of the Au surface, calculated for atoms in the first layer away from the perturbed region in the vicinity of the tip) are given by the letter symbols in Fig. 3, a and b. Note that the distance between the bottom of the tip and the gold atoms in the region immediately underneath it may differ from d_{ts}. Thus, for example, when $d_{hs} = 0$ (point D in Fig. 3, a and b) the tip to unperturbed gold distance, d_{ts}, is 3.8 Å, while the average distance between the bottom layer of the tip and the adherent gold layer in immediate contact with it is 2.1 Å.

Tip-sample approach. Comparison of Figs. 2a and 3a reveals similarity between the measured and calculated curves showing a monotonic increase in the magnitude of the attractive force as the tip approaches the sample and a hysteresis during separation. Note, however, that in the experiment (Fig. 2a) the magnitude of the force and the distance from the surface at which it begins to deviate from zero are much larger than in the calculated data (Fig. 3a). These differences are caused primarily by differences in tip size and to the neglect of long-range interactions (such as van der Waals forces) in the calculations. Also, in the experiment, it is difficult to determine

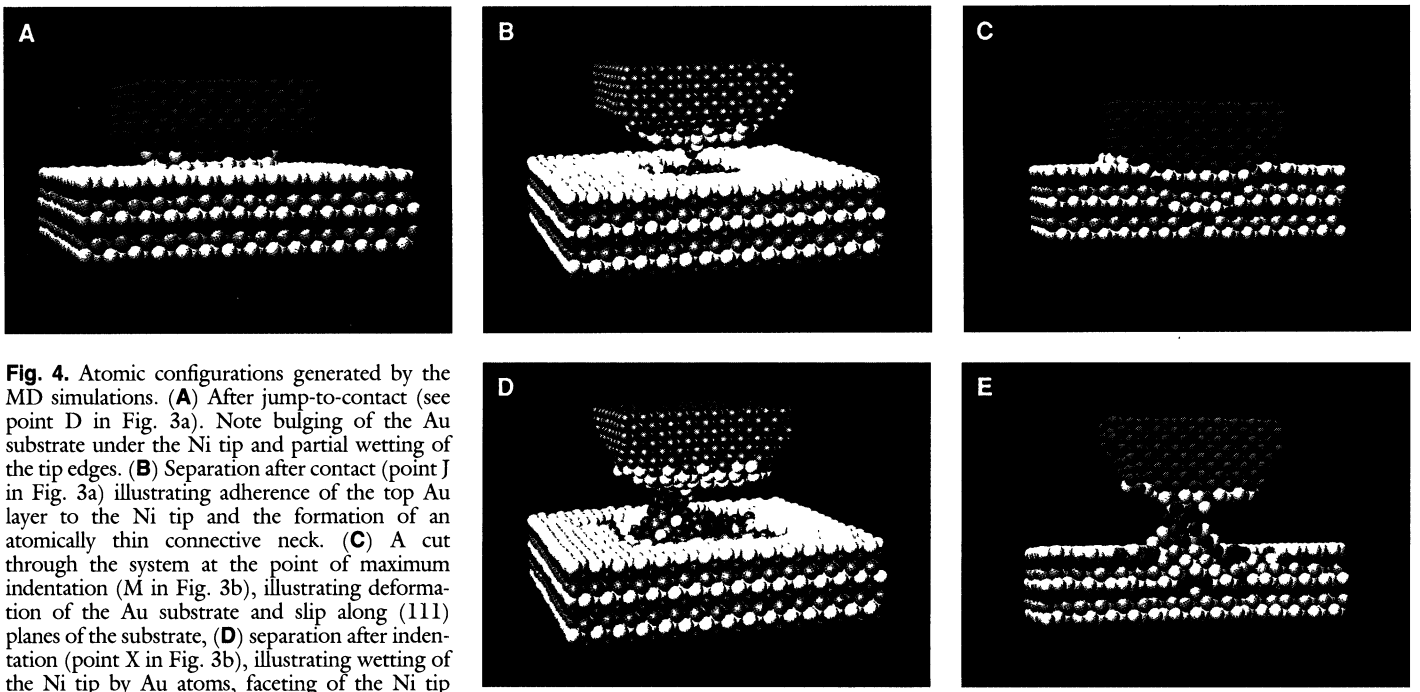

Fig. 4. Atomic configurations generated by the MD simulations. (**A**) After jump-to-contact (see point D in Fig. 3a). Note bulging of the Au substrate under the Ni tip and partial wetting of the tip edges. (**B**) Separation after contact (point J in Fig. 3a) illustrating adherence of the top Au layer to the Ni tip and the formation of an atomically thin connective neck. (**C**) A cut through the system at the point of maximum indentation (M in Fig. 3b), illustrating deformation of the Au substrate and slip along (111) planes of the substrate, (**D**) separation after indentation (point X in Fig. 3b), illustrating wetting of the Ni tip by Au atoms, faceting of the Ni tip exposing (111) facet planes, incorporation of Ni atoms in substitutional sites, and formation of an extensive connective neck between the tip and the substrate. Note the crystalline character of the neck and the incorporation of atoms from the first, second and third topmost layers of the Au surface as well as several Ni atoms. (**E**) A cut through the system shown in (D) illustrating the crystalline structure of the neck and the extent of structural deformations of the substrate. In these figures the Ni tip atoms are colored red; atoms of the top layer of the Au surface in yellow, second layer in blue, third layer in green, fourth in yellow, and so forth.

where the cantilever tip is in relation to the surface until contact has already been made. Therefore it is likely that a slight indentation has occurred in the data shown in Fig. 2a. This problem can be alleviated in future experiments by using phase-sensitive detection to denote contact and reverse the direction of the sample motion. Other differences between theory and experiment include tip or sample roughness and exposure to air during sample preparation. We stress that in our experiments cantilever-dependent instability has been ruled out as a possible origin of the observed hysteresis. Furthermore, hystersis in the piezoelectric actuators used in the instrument is negligible. Rather, the hystersis originates from dynamical processes induced by the tip-substrate adhesive interactions as revealed by the simulations.

Following an initial slow variation of the force between the Au substrate an the Ni tip we observe in the simulations the onset of an instability, signified by a sharp increase in the attraction between the two (see Fig. 3a as well as Fig. 3, b and c, where the segments corresponding to lowering of the tip up to the point D describe the same stage as that shown in segment AD in Fig. 3a) which is accompanied by a marked decrease in the potential energy of the system (see sudden drop of E_p in Fig. 3c as d_{hs} approaches zero from the right). We note the rather sudden onset of the instability which occurs only for separations d_{hs} smaller than 0.25 Å (marked by an arrow on the curve in Fig. 3a). Our simulations reveal that in response to the imbalance between the forces on atoms in each of the materials and those due to intermetallic interactions a JC phenomenon occurs via a fast process where Au atoms in the region of the surface under the Ni tip displace by approximately 2 Å toward the tip in a short time span of ~1 ps (see bulging of the gold surface shown in Fig. 4A where the atomic configuration after the JC is depicted). After the JC occurs the distance between the bottom layer of the Ni tip and the layer of adherent Au atoms in the region immediately underneath it decreases to 2.1 Å from a value of 4.2 Å. In addition to the adhesive contact formation between the two surfaces an adhesion-induced partial wetting of the edges of the Ni tip by Au atoms is observed (see Fig. 4A).

The JC phenomenon in metallic systems is driven by the marked tendency of the atoms at the interfacial regions of the tip and substrate materials to optimize their embedding energies (which are density-dependent, deriving from the tails of the atomic electronic charge densities) while maintaining their individual material cohesive binding (in the Ni and Au) albeit strained because of the deformation caused by the atomic displacements during the JC process. In this context we note the difference between the surface energies of the two metals, with the one for Ni markedly larger than that of Au.

Further insight into the JC process is provided by the local hydrostatic pressure in the materials [evaluated as the trace of the atomic stress tensors (*54*)] shown in Fig. 5a after contact formation (that is, point D in Fig. 3a). The pressure contours reveal that atoms at the periphery of the contact zone (at $X = \pm 0.19$ and $Z = 0.27$) are under extreme tensile stress (-10^5 atm $\simeq -10^{10}$ N/m^2 $= -10$ GPa). In fact we observe that the tip as well as an extended region of the substrate in the vicinity of the contact zone are under tension. Both the structural deformation profile of the system and the pressure distribution which we find in our atomistic MD simulations are similar, in general terms, to those described by certain modern contact mechanics theories (*21–24*) where the influence of adhesive interactions is included.

Tip-substrate separation after contact. Starting from contact the force versus distance (F_z versus d_{hs}) curve exhibits a marked hysteresis seen both experimentally (Fig. 2a) and theoretically (Fig. 3a) as the surfaces are separated. We remark that, in the simulation and the measurements, separating the surfaces prior to contact results in no

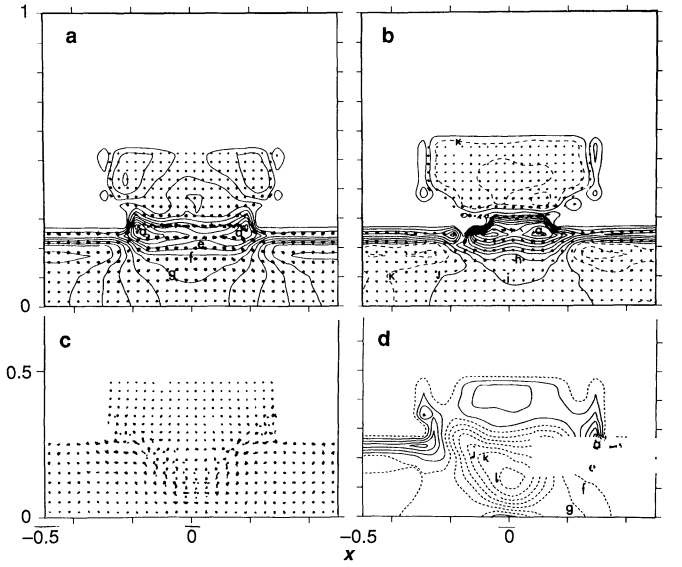

Fig. 5. Calculated pressure contours and atomic configurations viewed along the [010] direction, in slices through the system. The Ni tip occupies the topmost eight atomic layers. Short-time atomic trajectories appear as dots. Distance along the X and Z directions in units of $X = 1$ and $Z = 1$ corresponding to 61.2 Å each. Solid contours correspond to tensile stress (that is, negative pressure) and dotted ones to compressive stress. (**a**) After jump-to-contact (point D in Fig. 3a; see also Fig. 4A). The maximum magnitude of the tensile (that is, negative) pressure, −10 GPa, is at the periphery of the contact, $(X, Z) = (\pm 0.19, 0.27)$. The contours are spaced with an increment, Δ, of 1 GPa. Thus the contours marked e, f, and g correspond to −6, −5, and −4 GPa, respectively. (**b**) During separation following contact, (point G in Fig. 3a). The maximum tensile pressure (marked a), ~−9 GPa, is at the periphery of the contact at (X, Z) equal to (0.1, 0.25) and (−0.04, 0.25). $\Delta = 0.9$ GPa. The marked contours h, i, j, and k correspond to −2.5, −1.6, −0.66, and 0.27 GPa, respectively. (**c**) Short-time particle trajectories at the final stage of relaxation of the system, corresponding to point M in Fig. 3b (that is, $F_z = 0$). Note slip along the [111] planes in the substrate. (**d**) Pressure contours corresponding to the final configuration shown in (c). Note the development of compressive pressure in the substrate which maximizes in the region of the contour marked ℓ (8.2 GPa). The increment between contours $\Delta = 1.4$ GPa. The contours marked a and e correspond to −6.4 GPa and −1.1 GPa, respectively, and those marked f and g to 0.2 and 1.6 GPa.

hysteresis. The hysteresis is a consequence of the adhesive bonding between the two materials and, as demonstrated by the simulation, separation is accompanied by inelastic processes in which the topmost layer of the Au sample adheres to the Ni tip. (See the configuration shown in Fig. 4B which corresponds to the distance $d_{ts} = 7.5$ Å marked J in Fig. 3a.) The mechanism of the process is demonstrated by the pressure contours during liftoff of the tip shown in Fig. 5b, recorded for the configuration marked G ($d_{ts} = 5.5$ Å in Fig. 3a). As seen the maximum tensile stress is located near the edges of the adhesive contact. We further observe that the diameter of the contact area decreases during lifting of the tip, resulting in the formation of a thin "adhesive neck" arising from ductile extension, which stretches as the process continues, ultimately breaking at a distance d_{ts} of ~9 to 10 Å. The evolution of adhesion and tear mechanisms which we observe can be classified as mode-I fracture (*33*), reemphasizing the importance of forces operating across the crack in modeling crack propagation (*33, 34*).

Indentation. We turn now to theoretical and experimental results recorded when the tip is allowed to advance past the JC point, that is, indentation (see Figs. 2b, 3, b and c, and 4C). As evident from Fig. 3b, decreasing the separation between the tip and the substrate causes first a decrease in the magnitude of the force on the tip (that

is, less attraction; see segment DL) and an increase in the binding energy (that is, larger magnitude of the potential energy shown in Fig. 3c). However, upon reaching the point marked L in Fig. 3b a sharp increase in the attraction occurs, followed by a monotonic decrease in the magnitude of the force till $F_z = 0$ (point M in Fig. 3b) at $d_{ts} = 0.8$ Å. The variations of the force (in the segment DLM) are correlated with large deformations of the Au substrate (see the atomic configuration in Fig. 4C, corresponding to point M in Fig. 3b). In particular, the nonmonotonic feature (near point L) results from tip-induced flow of gold atoms which relieve the increasing stress by wetting of the sides of the tip. Indeed the atomic configurations (Figs. 4C and 5c) display a "piling-up" around the edges of the indenter attributable to atomic flow driven by the deformation of the Au substrate and the adhesive interactions between the Au and Ni atoms. Further indentation is accompanied by slip of Au layers [along (111) planes] and the generation of interstitial defects (see atomic trajectories and atomic configuration, corresponding to point M, in Figs. 4C and 5c, respectively). In addition, the calculations predict that during the indentation process a small number of Ni atoms diffuse into the surrounding Au, occupying substitutional sites. Furthermore the calculated pressure contours at this stage of indentation, shown in Fig. 5d, demonstrate that the substrate surface zone in the vicinity of the edges of the tip is under tensile stress, while the deformed region under the tip is compressed with the maximum pressure (8.2 GPa) occurring at about the fifth Au layer below the center of the Ni tip-indenter. The general characteristics of the pressure (and stress) distributions obtained in our indentation simulations correspond to those associated (*11, 21, 25*) with the onset and development of plastic deformation in the substrate.

Experimentally, advancing the sample past the contact point is noted by the change in slope of the force as the increasing repulsive forces push the tip and cantilever back towards their rest position, as shown in Fig. 2b. We remark that the calculated pressures from the simulations compare favorably with the average contact pressure of ~3 GPa determined experimentally (*47*) by dividing the measured attractive force by the estimated circular contact area of radius 20 nm.

Tip-substrate separation after indentation. Reversal of the direction of the tip motion relative to the substrate from the point of zero force (point M in Fig. 3b) results in the force and potential energy versus distance curves shown in Fig. 3, b and c. The force curve exhibits first a sharp monotonic increase in the magnitude of the attractive force (segment MN in Fig. 3b) with a corresponding increase in the potential energy (Fig. 3c). During this stage the response of the system is mostly elastic accompanied by the generation of a small number of vacancies and substitutional defects in the substrate. Past this stage the force and energy curves versus tip-to-sample separation exhibit a nonmonotonic behavior which is associated mainly with the process of elongation of the connective neck which forms between the substrate and the retracting tip.

To illustrate the neck formation and elongation process we show in Fig. 6 a sequence of atomic configurations corresponding to the maxima in the force curve (Fig. 3b, points marked O, Q, S, U, W, and X). As evident, upon increased separation between the tip-holder and the substrate a connective neck forms consisting mainly of gold atoms (see atomic configurations shown in Fig. 4, D and E). The mechanism of elongation of the neck involves atomic structural transformations whereby in each elongation stage atoms in adjacent layers in the neck disorder and then rearrange to form an added layer, that is, a more extended neck of a smaller cross-sectional area. Throughout the process the neck maintains a layered crystalline structure (see Figs. 4E and 6) except for the rather short structural transformation periods, corresponding to the sharp variations in the force curve, (see segments PQ, RS, TU, and VW in Fig. 3b) and the associated features in the calculated potential energy shown in Fig. 3c where the minima correspond to ordered layered structures after the structural rearrangements. We note that beyond the initial formation stage, the number of atoms in the connective neck region remains roughly constant throughout the elongation process.

Further insight into the microscopic mechanism of elongation of the connective neck can be gained by consideration of the variation of the second invariant of the stress deviator, J_2, which is related to the von Mises shear strain-energy criterion for the onset of plastic yielding (*18, 21*). Returning to the force and potential energy curves shown in Fig. 3, b and c, we have observed that between each of the elongation events (that is, layer additions, points marked Q, S, U, W, and X) the initial response of the system to the strain induced by the increased separation between the tip-holder and the substrate is mainly elastic (segments OP, QR, ST, and UV in Fig. 3b, and correspondingly the variations in Fig. 3c), accompanied by a gradual increase of $\sqrt{J_2}$, and thus the stored strain energy. The onsets of the stages of structural rearrangements are found to be correlated with a critical maximum value of $\sqrt{J_2}$ of about 3 GPa (occurring for states at the end of the intervals marked OP, QR, ST, and UV in Fig. 3b) localized in the neck in the region of the ensuing structural transformation. After each of the elongation events the maximum value of $\sqrt{J_2}$ (for the states marked Q, S, U, W, and X in Fig. 3b) drops to approximately 2 GPa.

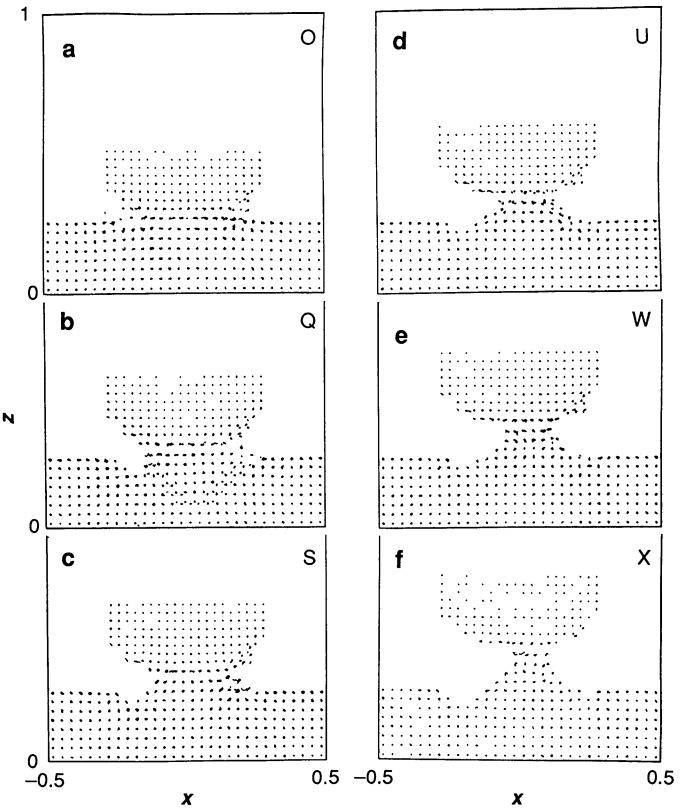

Fig. 6. Atomic configurations in slices through the system illustrating the formation of a connective neck between the Ni tip and the Au substrate during separation following indentation. The Ni tip occupies the topmost eight layers. The configurations (**a** through **f**) correspond to the stages marked O, Q, S, U, W, and X in Fig. 3b. Note the crystalline structure of the neck. Successive elongations of the neck, upon increased separation between the tip-holder assembly and the substrate, occur by way of a structural transformation resulting in successive addition of layers in the neck accompanied by narrowing (that is, reduction in cross-sectional area of the neck). Distance in units of X and Z, with $X = 1$ and $Z = 1$ corresponding to 61.2 Å.

In this context, it is interesting to remark that the value of the normal component of the force per unit area in the narrowest region of the neck remains roughly constant (~10 GPa) throughout the elongation process, increasing by about 20% prior to each of the aforementioned structural rearrangements. This value has been estimated both by using the data given in Figs. 3b and the cross-sectional areas from atomic configuration plots (such as given in Fig. 6), and via a calculation of the average axial component (zz element) of the atomic stress tensors (*54*) in the narrow region of the neck. We note that the above observations constitute atomic-scale realizations of basic concepts which underlie macroscopic theories of materials behavior under load (*17–21*).

A typical distribution of the stress, $\sqrt{J_2}$, prior to a structural transformation is shown in Fig. 7 (shown for the state corresponding to the point marked T in Fig. 3b). As seen, the maximum of $\sqrt{J_2}$ is localized about a narrow region around the periphery in the strained neck. Comparison between the atomic configuration at this stage (see Fig. 7, or the very similar configuration shown in Fig. 6c) and the configuration after the structural transformation has occurred (see Fig. 6d, corresponding to the point marked U in Fig. 3b) illustrates the elongation of the neck by the addition of a layer and accompanying reduction in areal cross section. We note that as the height of the connective neck increases the magnitude of the variations in the force and potential energy during the elongation stages diminishes. The behavior of the system past the state shown in Fig. 6f (corresponding to the point marked X in the force curve shown in Fig. 3b) is similar to that observed at the final stages of separation after JC (Fig. 3b), characterized by strain-induced disordering and thinning in a narrow region of the neck near the gold-covered bottom of the tip and eventual fracture of the neck (occurring for a tip-to-substrate distance $d_{ts} \simeq 18$ Å), resulting in an Ni tip whose bottom is covered by an adherent Au layer.

The theoretically predicted increased hysteresis upon tip-substrate separation following indentation, relative to that found after contact (compare Fig. 3, a and b), is also observed experimentally, as shown in Fig. 2b. In both theory and experiment the maximum attractive force after indentation is roughly 50% greater than when contact is first made. Note however that the nonmonotonic features found in the simulations (Fig. 3b) are not discernible in the experiment which is apparently not sufficiently sensitive to resolve such individual atomic-scale events when averaged over the entire contact area.

Finally we remark that scanning Auger microscopy (SAM) was used to detect gold transfer onto the nickel tip following indentation. The lack of sensitivity of SAM to concentrations of materials less than 0.1% prohibits us from detecting Au transfer onto the tip for the typical small loads used in the measurements discussed in this paper. However, we did observe the presence of Au on the Ni tip following the application of a load of ~100 mN between a freshly cleaned Ni tip and an Au surface, just moments before placing the tip into the Auger vacuum chamber for analysis.

Concluding Remarks

The recent emergence and proliferation of proximal probes, in particular tip-based microscopies (*35–38*), sensitive to nano- and subnanometer scale structures provides compelling opportunities for studies of these structures which are key to the science base of many venerable technological problems (*38*). In addition these probes, coupled with advances in theoretical understanding of the energetics and interaction mechanisms in materials and the development of computer-based materials modeling and simulation techniques, open new avenues for exploration of new scientific concepts and novel materials properties and processes on the subnanometer scale (*38, 55*).

In this paper we have presented results of joint theoretical, molecular dynamics simulations, and experimental, atomic force microscopy, studies of the mechanisms and properties of intermetallic adhesive interactions, contact formation, nanoindentation, and mechanical response. Our studies show that contact formation between a hard tip (nickel) approaching a soft metallic substrate (gold) is associated with an atomic-scale instability which leads to a JC phenomenon which involves an inelastic response of the atoms in the proximal interfacial region of the gold substrate. Indentation of the surface by advancing the tip beyond the point of contact results in the onset of plastic yielding, adhesion-induced atomic flow, and generation of slip in the surface region of the gold substrate. Separating the two materials from contact results in adhesion-induced wetting of the tip by gold atoms, adherence of a gold monolayer to the nickel tip, formation of an atomically thin connective neck, and eventual fracture. Furthermore, retracting the tip from the sample after indentation results in ductile extension of the substrate and formation of a connective crystalline neck which elongates, while reducing in cross-sectional area, by structural transformations involving elastic and yielding stages.

The above microscopic processes are portrayed in the theoretically calculated and experimentally measured force versus distance curves (Figs. 2 and 3), which exhibit pronounced hysteresis upon tip-to-sample approach and subsequent separation. We note, however, that because of experimental constraints (such as the need to employ a cantilever of finite flexibility, sample and tip cleanliness, and tip size) certain characteristic features predicted by the simulations (that is, the nonmonotonic behavior of the force versus distance relationship during separation after indentation, associated with atomic structural transformations during elongation of the connective neck) could not be resolved in the present measurements.

Our investigations provide the impetus for further combined theoretical and experimental investigations of the microscopic mechanisms of adhesion, contact formation, and atomic-scale mechanical response processes in materials, motivating a critical assessment of the range of validity of continuum theories and reformulation of contact mechanics formalisms (*10, 21, 56*) to incorporate an atomistic description of the processes of adhesion, deformation, wetting, and fracture. In addition, the results presented here are pertinent to the general issue of the consequences of tip-substrate interactions in tip-based microscopies (STM and AFM) and for studies of the transition from tunneling to point contact in STM (*12, 13, 57–59*).

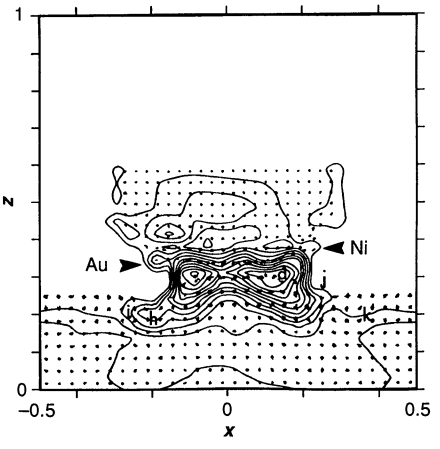

Fig. 7. Von Mises' shear stress ($\sqrt{J_2}$) corresponding to the configuration marked T in Fig. 3b [that is, just before the structural transformation resulting in the configuration (d) in Fig. 6]. The proximal interfacial layers of Ni and Au are marked by arrows. The maximum contours (2.9 GPa, marked a) occur on the periphery of the neck (X, Z) = (±0.1, 0.3). The increment between contours is 0.2 GPa. The contours marked h, i, j, and k correspond to 1.1, 0.9, 0.7, and 0.5 GPa, respectively. Distance along X and Z in units of X = 1 and Z = 1 corresponding to 61.2 Å.

Finally, our studies suggest a method for preparation of atomic size contacts and atomically thin wires (by the process of contact formation between a metallic tip and a soft metal substrate, followed by gentle separation) which could be used to study conductance (and quantum effects) in narrow constrictions (*60*).

REFERENCES AND NOTES

1. D. Tabor, *J. Coll. Interface Sci.* **58**, 2 (1977); M. D. Pashley and D. Tabor, *Vacuum* **31**, 619 (1981).
2. N. Gane, P. F. Pfaelzer, D. Tabor, *Proc. R. Soc. London A* **340**, 395 (1974).
3. H. M. Pollock, *Vacuum* **31**, 609 (1981).
4. D. Maugis, *Le Vide* **186**, 1 (1977).
5. R. G. Horn, J. N. Israelachivili, F. Pribac, *J. Coll. Interface Sci.* **115**, 480 (1987) and references therein.
6. N. A. Burnham and R. J. Colton, *J. Vac. Sci. Technol.* **A7**, 2906 (1989).
7. U. Landman, W. D. Luedtke, R. N. Barnett, in *Many-Atom Interactions in Solids*, R. M. Nieminen, Ed. (Plenum, NY, 1989), where a preliminary report of the theoretical studies can be found.
8. D. Tabor and R. H. S. Winterton, *Proc. R. Soc. London A* **312**, 435 (1969).
9. H. M. Pollock, P. Shufflebottom, J. Skinner, *J. Phys. D* **10**, 127 (1977); H. M. Pollock, *ibid.* **11**, 39 (1978).
10. N. Gane and F. P. Bowden, *J. Appl. Phys.* **39**, 1432 (1968).
11. D. Maugis and H. M. Pollock, *Acta Metall.* **32**, 1323 (1984), and references therein.
12. U. Durig, J. K. Gimzewski, D. W. Pohl, *Phys. Rev. Lett.* **57**, 2403 (1986); U. Durig, O. Zuger, D. W. Pohl, *J. Microsc.* **152**, 259 (1988).
13. J. M. Gimzewski and R. Moller, *Phys. Rev. B* **36**, 1284 (1987).
14. J. B. Pethica and A. P. Suttom, *J. Vac. Sci. Technol.* **A6**, 2494 (1988).
15. J. R. Smith, G. Bozzolo, A. Banerjea, J. Ferrante, *Phys. Rev. Lett.* **63**, 1269 (1989).
16. U. Landman, W. D. Luedtke, M. W. Ribarsky, *J. Vac. Sci. Technol.* **A7**, 2829 (1989); *Mater. Res. Soc. Symp. Proc.* **140**, 101 (1989); see also M. W. Ribarsky and U. Landman, *Phys. Rev. B* **38**, 9522 (1988).
17. H. Hertz, *J. Reine Angew. Math.* **92**, 156 (1882); also in *Miscellaneous Papers* (Macmillan, London, 1896), p. 146; see review by K. L. Johnson, *Proc. Instn. Mech. Engrs.* **196**, 363 (1982).
18. G. Dieter, *Mechanical Metallurgy* (McGraw-Hill, New York, 1967).
19. E. Rabinowicz, *Friction and Wear of Materials*, (Wiley, New York, 1965).
20. S. P. Timoshenko and J. N. Goodier, *Theory of Elasticity* (McGraw-Hill, New York, ed. 3, 1970).
21. K. L. Johnson, *Contact Mechanics* (Cambridge Univ. Press, Cambridge, 1985).
22. ———, K. Kendall, A. D. Roberts, *Proc. R. Soc. London A* **324**, 301 (1971).
23. B. V. Derjaguin, V. M. Muller, Yu. P. Toporov, *J. Coll. Interface Sci.* **53**, 314 (1975); V. M. Muller, B. V. Derjaguin, Yu. P. Toporov, *Colloids Surfaces* **7**, 251 (1983).
24. P. A. Pashley, *Colloids Surfaces* **12**, 69 (1984).
25. D. Tabor, *The Hardness of Metals* (Clarendon Press, Oxford, 1951).
26. J. B. Pettica, R. Hutchings, W. C. Oliver, *Philos. Mag.* **A48**, 593 (1983).
27. N. Gane, *Proc. R. Soc. London A* **317**, 367 (1970), and references therein.
28. P. J. Blau and B. R. Lawn, Eds., *Microindentation Techniques in Materials Science and Engineering* (American Society for Testing and Materials, Philadelphia, 1985).
29. M. F. Doerner and W. D. Nix, *J. Mater. Res.* **1**, 601 (1988).
30. See articles in *Mater. Res. Soc. Symp. Proc.* **140**, 101 (1989), edited by L. E. Pope, L. L. Fehrenbacher and W. O. Winer (Materials Research Society, Pittsburgh, 1989); F. P. Bowden and D. Tabor, *Friction and Lubrication Solids* (Clarendon Press, Oxford, 1950).
31. C. W. Mate, G. M. McClelland, R. Erlandsson, S. Chiang, *Phys. Rev. Lett.* **59**, 1942 (1987).
32. U. Landman, W. D. Luedtke, A. Nitzan, *Surf. Sci.* **210**, L177 (1989).
33. R. Thomson, *Solid State Phys.* **9**, 1 (1986).
34. B. R. Lawn, *Appl. Phys. Lett.* **47**, 809 (1985).
35. G. Binning, C. F. Quate, Ch. Gerber, *Phys. Rev. Lett.* **56**, 930 (1986).
36. J. N. Israelachvili, *Acc. Chem. Res.* **20**, 415 (1987); *Proc. Nat. Acad. Sci. U.S.A.* **84**, 4722 (1987); J. N. Israelachvili, P. M. McGuiggan, A. M. Homola, *Science* **240**, 189 (1988).
37. G. Binning, H. Rohrer, Ch. Gerber, E. Weibel, *Phys. Rev. Lett.* **50**, 120 (1983).
38. See reviews by: P. K. Hansma and J. Tersoff, *J. Appl. Phys.* **61**, R1 (1986); R. J. Colton and J. S. Murday, *Naval Res. Rev.* **40**, 2 (1988); J. S. Murday and R. J. Colton, *Mater. Sci. Eng. B*, in press; J. S. Murday and R. J. Colton in *Chemistry and Physics of Solid Surfaces. VIII*, R. Vanselow and R. Howe, Eds, Springer Ser. Surf. Sci. (Springer, Berlin, 1990).
39. See articles in *Atomistic Simulation of Materials: Beyond Pair Potentials*, V. Vitek and D. J. Srolovitz, Eds. (Plenum, New York, 1989).
40. See reviews by: F. F. Abraham, *Adv. Phys.* **35**, 1 (1986); *J. Vac. Sci. Technol.* **B2**, 534 (1984); U. Landman, in *Computer Simulation Studies in Condensed Matter Physics: Recent Developments*, D. P. Landau, K. K. Mon, H.-B. Schuttler, Eds. (Springer, Berlin, 1988), p. 108.
41. M. D. Pashley, J. B. Pethica, D. Tabor, *Wear* **100**, 7 (1984).
42. F. F. Abraham, I. P. Batra, S. Ciraci, *Phys. Rev. Lett.* **60**, 1314 (1988).
43. R. J. Colton *et al.*, *J. Vac. Sci. Technol.* **A6**, 349 (1988).
44. D. Tomanck, C. Overney, H. Miyazaki, S. D. Mahanti, H. J. Guntherodt, *Phys. Rev. Lett.* **63**, 876 (1989).
45. J. M. Soler, A. M. Baro, N. Garcia, H. Rohrer, *ibid.* **57**, 444 (1986); see comment by J. B. Pethica, *ibid.*, p. 3235.
46. J. B. Pethica and W. C. Oliver, *Phys. Scripta* **T19**, 61 (1987).
47. N. A. Burnham, D. D. Dominguez, R. L. Mowery, R. J. Colton, *Phys. Rev. Lett.*, in press.
48. *Mater. Eng.* **90**, C120 (1979).
49. S. M. Foiles, M. I. Baskes, M. S. Daw, *Phys. Rev. B* **33**, 7983 (1986).
50. The parameterization used in our calculations is due to J. B. Adams, S. M. Foiles, W. G. Wolfer, *J. Mater. Res. Soc.* **4**, 102 (1989).
51. See review by M. Baskas, M. Daw, B. Dodson, S. Foiles, *Mater. Res. Soc. Bull.* **13**, 28 (1988).
52. E. T. Chen, R. N. Barnett, U. Landman, *Phys. Rev. B* **40**, 924 (1989); *ibid.* **41**, 439 (1990).
53. R. N. Barnett, U. Landman, C. L. Cleveland, *ibid.* **28**, 1685 (1983).
54. T. Egami and D. Srolovitz, *J. Phys.* **12**, 2141 (1982).
55. R. P. Feynman, in *Miniaturization*, H. D. Gilbert, Ed. (Reinhold, New York, 1961), p. 282.
56. Q. Guo, J. D. J. Ross, H. M. Pollock, *Mater. Res. Soc. Proc.* **140**, 51 (1989).
57. N. D. Lang, *Phys. Rev. B* **36**, 8173 (1987); *Comments Condens. Matter Phys.* **14**, 253 (1989).
58. B. J. van Wees *et al.*, *Phys. Rev. Lett.* **60**, 848 (1988); D. A. Wharam *et al.*, *J. Phys. C* **21**, L209 (1988).
59. J. K. Gimzeski, R. Moller, D. W. Pohl, R. R. Schlittler, *Surf. Sci.* **189/190**, 15 (1987).
60. N. D. Lang, A. Yacoby, Y. Imry, *Phys. Rev. Lett.* **63**, 1499 (1989), and references therein.

61. The authors thank I. Singer, H. Pollock, N. Turner, and the STM group (S. Brandow, R. Brizzolara, D. DiLella, K. Lee, and C. Marrian) for their suggestions and helpful discussions. We thank C. L. Cleveland for most valuable assistance with the generation of computer graphics, V. P. Mallette for excellent photography, and A. Ralston for meticulous typing. We would like to thank the Department of Energy, National Science Foundation, Air Force Office of Scientific Research (U.L.), and Office of Naval Research (R.J.C.) for support of this work. Simulations were performed on the Cray Research, Inc., computers at the National Magnetic Fusion Energy Computing Center, Livermore, CA, through a grant from DOE. This work was done while N.A.B. held a National Research Council–Naval Research Laboratory Research Associateship.